American Mineralogist, Volume 102, pages 1622–1631, 2017

SPECIAL COLLECTION: FROM MAGMAS TO ORE DEPOSITS

Physicochemical controls on bismuth mineralization: An example from Moutoulas, Serifos Island, Cyclades, Greece

Michalis Fitros[1,*], Stylianos F. Tombros[1], Anthony E. Williams-Jones[2], Basilios Tsikouras[1,3], Eleni Koutsopoulou[1], and Konstantin Hatzipanagiotou[1]

[1]Department of Geology, Section of Earth Materials, University of Patras, Rion, 26500, Patras, Greece
[2]Department of Earth and Planetary Sciences, 3450 University Street, Montreal, Quebec H3A 2A7, Canada
[3]Faculty of Science, Physical and Geological Sciences, Universiti Brunei Darussalam, Jalan Tungku Link, BE1410 Gadong, Bandar Seri Begawan, Brunei Darussalam

Abstract

The 11.6 to 9.5 Ma Serifos pluton intruded schists and marbles of the Cycladic Blueschist unit, causing thermal metamorphism, the development of magnetite Ca-exo- and endo-skarns and the formation of low-temperature vein and carbonate-replacement ores. Potentially, the most important ores occur in the Moutoulas prospect where the mineralization in retrograde skarn and quartz veins culminated with the deposition of native bismuth. A combination of fluid inclusion microthermometry and isotope geothermometry suggests that the Moutoulas mineralization formed at a hydrostatic pressure of ~100 bars, from moderate-to-low temperature (~190–250 °C), and low-salinity (1.3–5.6 wt% NaCl equivalent) fluids. The calculated $\delta^{34}S_{H_2S}$ compositions are consistent with the ore fluids having been derived from the Serifos pluton. Bismuth mineralization is interpreted to have occurred as a result of wall-rock interaction and mixing of a Bi-bearing ore fluid with meteoric waters. Native bismuth and bismuthinite deposited at ~200 °C, near neutral pH (6.5), low f_{S_2} (< -16.5), and low f_{O_2} (< -44). Supergene alteration in Serifos led to the oxidation of native bismuth to bismite and bismutite.

Keywords: Native bismuth, retrograde skarn, supergene alteration, Moutoulas, Serifos

Rabillard et al. 2015). The following lithotypes of UCU occur in Serifos (Fig. 1): calcitic marbles, ankerite-dolomite-talc-goethite carbonate-replacement orebodies, meta-basites, and serpentinites (Grasemann and Petrakakis 2007; Petrakakis et al. 2007). The lower Megalo Livadi detachment (ML) separates the CB from the CBU, and the upper Kavos Kiklopas detachment (KK) separates the CBU from the UCU (Grasemann et al. 2012; Ducoux et al. 2017; Fig. 1).

The Serifos pluton was emplaced at ~11.6 to 9.5 Ma in the CB and CBU rocks along the NE-SW trending ML detachment, creating a contact metamorphic aureole, 0.5 to 1 km in width (Fig. 1, Rabillard et al. 2015). I-type, hornblende-biotite granodiorite with subordinate tonalite intruded at its center, and granodiorite to S-type hornblende-biotite-allanite-zinnwaldite granite at its margins (Stouraiti and Mitropoulos 1999; Grasemann and Petrakakis 2007; Seymour et al. 2009). The pluton crystallized at a temperature of ~700 to 750 °C and was emplaced at a pressure of 0.15 to 0.35 GPa (Seymour et al. 2009). Granodioritic to granitic apophyses, zoned pegmatites, aplites, and dacitic dikes intruded the CBU rocks along NW-SE trending, counterclockwise reverse faults (Fig. 1). Their ages range from 8.2 to 8.7 Ma (Altherr et al. 1982), and they formed at $T \leq 650$ °C and $P = 0.1$–0.2 GPa (Stouraiti and Mitropoulos 1999; Seymour et al. 2009).

Pyroxene-garnet exoskarns occur in the CBU marbles and garnet- and pyroxene-garnet endoskarns in the pluton (Ducoux et al. 2017; Fig. 1). The exoskarns comprise diopside-hedenbergite, andradite, wollastonite, and magnetite and minor suanite ($Mg_2B_2O_5$) (Salemink 1985; Seymour et al. 2009; Fig. 1). Formation of ore minerals in the Serifos exoskarn began with the deposition of high-temperature magnetite at the contact of the pluton with the CBU (Fig. 1). Subsequent retrograde skarn formation at Moutoulas (~1 km from the pluton contact, Fig. 1) resulted in the precipitation of pyrite, sphalerite, chalcopyrite, galena, and native bismuth. The mineralization takes the form of lenses up to 0.5 × 40 × 25 m in size that mainly replaced the CBU marbles, and it is interpreted to represent an early carbonate replacement event (Seymour et al. 2009). Four major syntaxial quartz veins trending NNW-SSE (up to 100 m long and 0.5 m wide) cross-cut the CBU schists and marbles and are surrounded by alteration halos comprising an inner silica + sericite + pyrite ± calcite zone (replacing orthoclase and albite of the CBU schists) and an outer epidote ± chlorite, barite, pyrite, and galena zone (Fig. 2a). The magnetite and sulfide ores underwent later supergene oxidation.

Analytical methods

The ore minerals were identified using a combination of reflected light microscopy and X-ray diffraction (XRD) on a D8 Advance diffractometer (Bruker AXS) equipped with a LynxEye strip silicon detector. The X-ray diffractometer employed Ni-filtered Cu*K*α radiation, a voltage of 35 kV, a 35 mA current, and 0.298° divergence and antiscatter slits. Random powder mounts of samples were scanned from 2 to 70° 2θ with a scanning step of 0.015° 2θ, and with 18.7 s count time per step, at the Research Laboratory of Minerals and Rocks, Department of Geology, University of Patras, Greece. Data were evaluated with the DIFFRACplus EVA v12.0 software and were compared with the PDF-2 database (ICDD, Newtown Square, Pennsylvania, U.S.A.).

Ore mineral compositions were determined using a JEOL 8900 Superprobe equipped with energy- and wavelength-dispersive spectrometers (EDS and WDS, respectively) and an xClent system for parts per million level resolution, at the Microprobe Center of the Department of Earth and Planetary Sciences Department, McGill University. The operating conditions were an acceleration voltage of 15kV, a beam current of 10 nA, and counting time of 20 s for all elements except Ag, As, and Te for which the counting times were 100 and 50 s, respectively. The standards used were natural chalcopyrite, tetrahedrite, tennantite, stibnite, pyrite, sphalerite, and galena, synthetic CoNiAs, SnO_2, and CdTe, and the native metals Ag, Au, and Se. Minimum detection limits were 200 ppm for S; 300 ppm for Mn, Cd, and Se; 400 ppm for Ag, Te, and Au; 500 ppm for Zn, Fe, and Co; 600 ppm for Sb and Bi; 700 ppm for Cu and As; and 2000 ppm for Pb.

Microthermometric measurements were performed on two doubly polished 50–100 µm thick wafers in which clear quartz was in intergrowth with pyrite, sphalerite, or native bismuth. The Linkam MDSG600 heating-freezing stage coupled to a ZEISS microscope in the Department of Earth Sciences and Resources, China University of Geosciences, Beijing, China, was used for this purpose. Temperatures were measured with an alumel-chromel thermocouple and the readings were calibrated with synthetic inclusions at –56.6 °C (triple point of CO_2), 0.0 °C (melting point of ice), and +374.1 °C (critical point of H_2O). Freezing-heating rates were maintained between 0.2 and 5 °C/min and measurements were accurate to ±0.1 °C. Microthermometric data were reduced using the FLINCOR software (Brown 1989).

A subset of the fluid inclusions was analyzed using Laser Raman spectroscopy. This was done prior to microthermometric analysis in the Beijing Research Institute of Uranium Geology, China. The inclusions were analyzed for the common gases, mono- and poly-atomic ions and molecules via gas and ion chromatography. Gaseous composition was measured via a LabRAM HR800 Raman spectroscopic microscope, with a laser beam spot size of ~1 µm. The instrument recorded peaks ranging from 100–4000 cm^{-1} with a spectral resolution of 1–2 cm^{-1}, and their peaks identified using the reference catalog of Frezzotti et al. (2012). The relative concentrations (in mol%) of these species were calculated from the equations of Frezzotti et al. (2012) and the cross-sectional scattering coefficients of Dhamelincourt et al. (1979), using the LabSpec software. Liquid composition analysis was carried out with a Shimadzu HIC-SP Super ion chromatograph on double distilled water leaches using the method of Yardley et al. (1993). The analytical precision for all gases analyzed was ±1%, whereas for the cations and anions ±0.1 ppm.

Fifteen sulfide mineral samples were analyzed for their sulfur isotope compositions. Only crystals of a given sulfide in textural equilibrium with contiguous crystals were selected for analysis to be used for geothermometry. These crystals were handpicked after examination under a binocular microscope to ensure textural equilibrium and a purity of ≥98%. Isotopic compositions of sulfur were analyzed with a VGMM602E double collector mass spectrometer at the Chinese Academy of Geological Sciences (CAGS), Beijing, China. Sulfur from vein pyrite, chalcopyrite, sphalerite, greenockite, and galena was released using the method of Fritz et al. (1974). The sulfur isotopic ratios are reported in standard δ notation per mil relative to V-CDT. Analytical precision was better than ±0.2‰ for $\delta^{34}S$. We used the AlphaDelta software (Beaudoin and Therrien 2009) to compute the isotopic fractionation factors and temperatures for mineral pairs in isotopic equilibrium. In addition, we analyzed pyrite and galena for their lead isotope compositions. Lead isotopic compositions were determined using an England Nu Plasma High Resolution type MC-ICP-MS with standard NBS-981, following the method of Yuan et al. (2013). Long-term repeated measurements of lead isotopic ratios of standard NBS981 yielded $^{206}Pb/^{204}Pb = 16.9397 \pm 0.001$ and $^{207}Pb/^{204}Pb = 15.4974 \pm 0.001$ (all errors are reported at ±2σ).

The Moutoulas mineralization

Examination of the quartz veins reveals four distinct paragenetic stages of hydrothermal mineralization that can be recognized on the basis of mineralogical and textural relations (Fig. 2b, Table 1). The stage I assemblage occupies the margins of the veins and is characterized by massive, brecciated aggregates of subhedral pyrite with intergrowths of minor arsenopyrite, sphalerite ($X_{FeS\%} = 20.7$–25.8), chalcopyrite, and pyrrhotite (Figs. 2b, 3a, and 3b). Pyrite crystals incorporate appreciable amounts of Bi as submicroscopic grains of bismuthinite (Supplemental[1] Table 1). Stage II is represented by Bi- and Te-rich tetrahedrite-tennantite solid solutions ($X_{As\%} = 1.9$ to 2.3) and sphalerite ($X_{FeS\%} = 13.8$–18.7) filling brecciated pyrite (Fig. 3c, Supplemental[1] Table 1), as well as minor greenockite and gersdorffite. Frequently, tetrahedrite-tennantite is observed

[1]Deposit item AM-17-86125, Supplemental Material. Deposit items are free to all readers and found on the MSA web site, via the specific issue's Table of Contents (go to http://www.minsocam.org/msa/ammin/toc/2017/Aug2017_data/Aug2017_data.html).

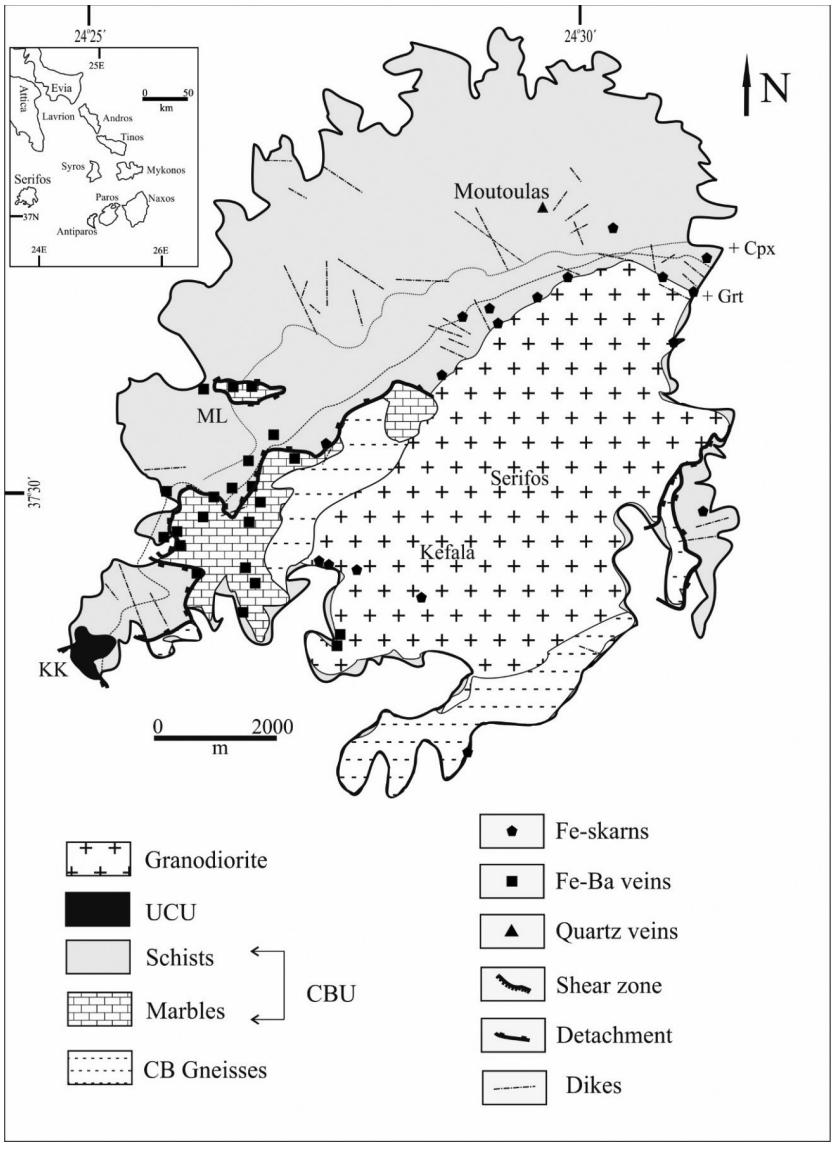

FIGURE 1. Simplified geological map of Serifos Island with the locations of magnetite exo- and endo-skarns, hematite ores, and sulfides (modified after Salemink 1985; Grasemann and Petrakakis 2007; Rabillard et al. 2015). The triangle represents the location of Figure 2.

to have replaced pyrite from stage I (Fig. 3c). Stage III occurs toward the vein center and consists of Bi-bearing galena, which intergrows with fluorite and calcite and replaces stage I and II minerals (Fig. 3d, Supplemental[1] Table 1).

The stage IV assemblage develops in three sub-stages, as disseminations replacing stage III galena in the central parts of the veins (Figs. 2c, 3e, and 3f; Table 1; Supplemental[1] Table 1). Calcite, fluorite, and barite also represent this stage. The early sub-stage includes euhedral acicular bismuthinite (Fig. 3e). The middle sub-stage comprises tellurides, including tetradymite, hessite, and melonite, and is succeeded by the late sub-stage that is dominated by native bismuth (Figs. 3e and 3f). In places, native bismuth replaced bismuthinite (Fig. 3f). During subsequent supergene alteration, mixtures of beyerite, bismutite, and bismite replaced native bismuth (Figs. 2c, 3e, 3f, and 4; Supplemental[1] Table 1). Covellite, cerussite, anglesite, chalcocite, goethite, azurite, and malachite also are products of this supergene stage (Table 1, data not shown).

RESULTS

Fluid inclusion studies

Fluid inclusion data were obtained for two undeformed samples containing clear quartz and sphalerite; the data are for stages I and IV. The analyzed fluid inclusions assemblages (FIAs) occur individually or as small randomly oriented clusters (4–10 μm in diameter). These inclusions are considered as primary in origin following the criteria of Roedder (1984). Their shapes include elliptical, negative crystal, and irregular forms without signs of necking down (Figs. 4a and 4b). Inclu-

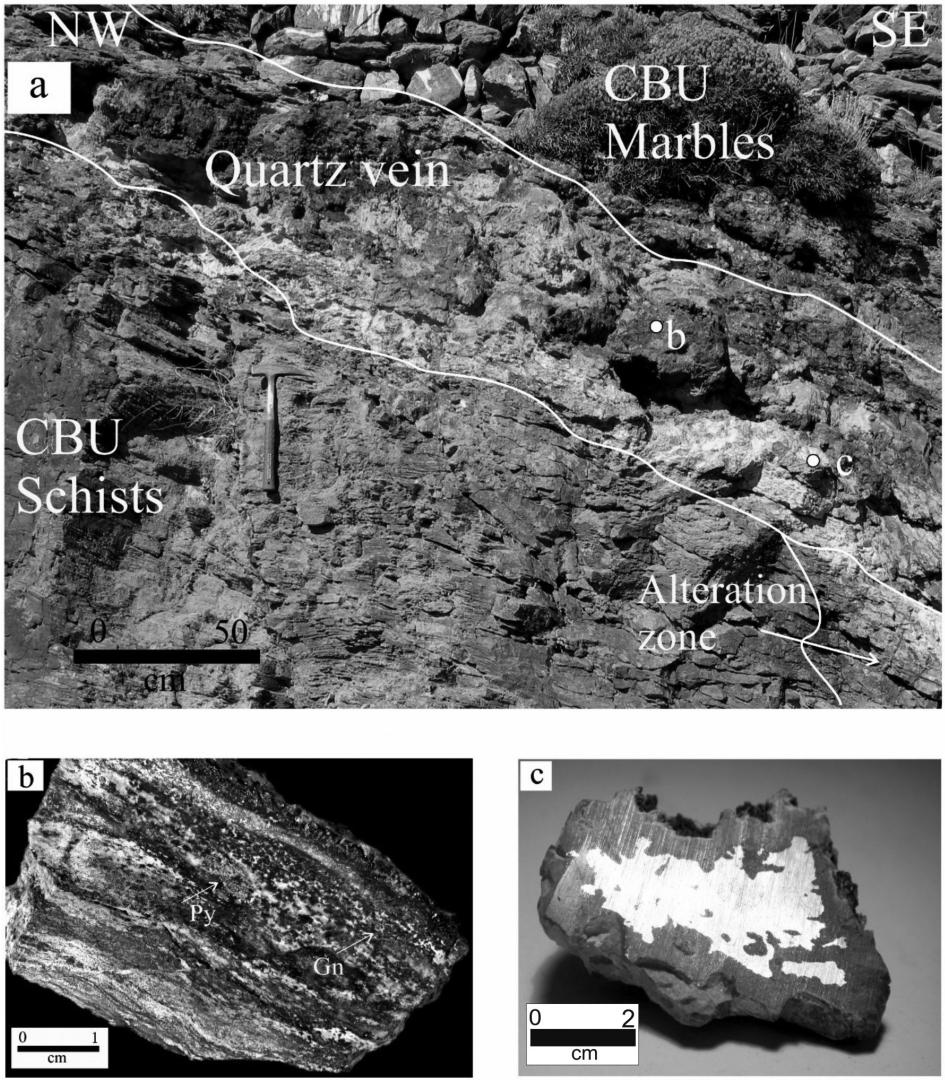

FIGURE 2. (**a**) A view of a sheared quartz vein at the interface between CBU schists and marbles containing the Bi-bearing assemblages studied. A bleached alteration halo is also evident. Also shown are the sampling sites (**b** and **c**). (**b**) A hand specimen of the vein containing pyrite (Py) and galena (Gn) (scale bar = 1 cm). (**c**) Native bismuth (Bi) rimmed by a supergene assemblage (S) of beyerite, bismutite, and bismite (scale bar = 2 cm).

sions were considered to be secondary if they occur in planar arrays interpreted to be healed fractures that do not terminate at growth zones or grain boundaries (Figs. 4a and 4b).

At room temperature, only one type of fluid inclusions was recognized, namely L-V inclusions, consisting of aqueous liquid and vapor, with the liquid being dominant (accounting for ~90 vol% of the total fluid inclusion volume; Supplemental[1] Table 2, Fig. 4b). Neither daughter crystals, trapped solids nor clathrates were observed. The temperature of initial melting of ice ranged from –23.8 to –21.1 °C and the temperature of last melting of ice from –3.7 to –2.1 °C (Supplemental[1] Table 2). Using the software FLINCOR (Brown 1989) for the system H_2O-NaCl (their initial melting temperatures are similar to the eutectic temperature of the system NaCl-H_2O), the corresponding salinities are 1.3 to 5.6 wt% NaCl equivalent (Supplemental[1] Table 2, Fig. 5). The inclusions homogenize to liquid between 190 and ~ 250 °C (Supplemental[1] Table 2, Fig. 5). As the pressure corresponding to the interpreted depth of emplacement of the Serifos pluton is interpreted to have been 3 to 12 km (Seymour et al. 2009), the trapping temperature of the inclusions was estimated to be ~5 °C higher than the homogenization temperature (corrected by the FLINCOR software). To fully constrain the density and pressure of entrapment (hydrostatic) of the fluid we made use of the Package FLUIDS (Bakker 2012). The calculated hydrothermal trapping pressures for the L-V inclusions vary from 80 to 140 bars, and average 105 bars (s.d. = 10 bars). The fluid densities range from 0.84 to 0.90 g/mL.

Raman spectroscopy and gas chromatography

Laser Raman and bulk composition chromatographic analyses were conducted on four L-V fluid inclusions hosted by stage I

TABLE 1. Ore paragenesis and vein fill minerals from Moutoulas area, Serifos

Mineral stages	Stage I	Stage II	Stage III	Stage IV[A]	Supergene stage
T (°C)	250			200	
Clear quartz					
Calcite					
Beyerite					
Barite					
Fluorite					
Pyrite					
Sphalerite	[a]	[b]			
Chalcopyrite					
Arsenopyrite					
Pyrrhotite					
Tetrahedrite-tennantite and s.s.		[c]			
Greenockite					
Gersdorffite					
Galena					
Bismuthinite[E]					
Tetradymite[M]					
Hessite[M]					
Melonite[M]					
Native bismuth[L]					
Bismutite					
Bismite					
Covellite					
Cerussite					
Anglesite					
Chalcocite					
Goethite					
Azurite					
Malachite					

Notes: Chemical formulas: bismuthinite (Bi_2S_3), tetradymite (Bi_2Te_2S), and melonite ($NiTe_2$), beyerite [$Ca(BiO)_2(CO_3)_2$], bismutite [$Bi_2O_2(CO_3)$], bismite (Bi_2O_3). The boxes represent the abundance. [A] Stage IV composes of three sub-stages, i.e., [E] Early, [M] Middle, and [L] Late sub-stage.
[a] $X_{FeS\%} = 25.8$, [b] $X_{FeS\%} = 13.8$, [c] $X_{As} = 1.9$ to 2.3.

and IV clear quartz that had been analyzed microthermometrically (Supplemental[1] Tables 3 and 4, Fig. 4b). Raman analyses reveal that the gaseous fluid phase is composed of H_2O, CO_2, O_2, H_2, and H_2S. The $\log X_{CO2/H2O}$, $\log X_{O2/H2O}$, and $\log X_{H2S/H2O}$ ratios range from of –1.0 to –0.8, –2.4 to –1.8, and –3.5 to –1.7, respectively. Also, to estimate temperature we have used the CO_2- and CO_2/H_2S-geothermometers of Arnórsson and Gunnlaugsson (1985) and Nehring and D'Amore (1984). The calculated temperatures for stages I and IV are 235–248 and 190–197 °C, respectively.

Bulk analyses of the liquid phase showed that it contained the cations Na^+, K^+, Mg^{2+}, Ca^{2+}, Si^{4+}, and the anions Cl^-, SO_4^{2-}, and HCO_3^-. Si^{4+} and HCO_3^- are the dominant ions in solution. These data allowed us to estimate the temperatures for the stages I and IV based on the Na-K-Ca geothermometer of Fournier and Truesdell (1973). The temperatures obtained were ~241 and 191–195 °C.

Isotope geochemistry

Sulfur isotopes. Sulfur isotope analyses were conducted on pyrite, sphalerite, chalcopyrite, greenockite, and galena (Table 2). The $\delta^{34}S_{V\text{-}CDT}$ isotopic values of stage I pyrite, sphalerite, and chalcopyrite range from 2.7 to 5.1‰. Values of $\delta^{34}S_{V\text{-}CDT}$ for stage II sphalerite and greenockite and III galena, were generally higher, i.e., 3.5, 5.5, and 5.0 to 5.6‰, respectively (Table 2). Temperatures of 249 ± 2 °C and 226 °C were calculated for stage I and stage II from the pyrite-sphalerite and sphalerite-greenockite isotopic pairs, respectively, utilizing the equations of Ohmoto and Rye (1979), Ohmoto and Lasaga (1982), and Li and Liu (2006). The calculated $\delta^{34}S_{H2S}$ values of the mineralizing fluid range from 2.3 to 4.9‰ (stage I, pyrite, sphalerite, and chalcopyrite), 3.1 to 4.8‰ (stage II, sphalerite and greenockite), and 2.4 to 2.8‰ (stage III, galena) (Table 2). These $\delta^{34}S_{H2S}$ values reflect a dominantly magmatic source for sulfur for the ore fluids, i.e., the Serifos granodiorite.

Lead isotopes. Lead isotope data were obtained for stage I pyrite and stage III galena. Their $^{206}Pb/^{204}Pb$ and $^{207}Pb/^{204}Pb$ ratios range from 18.806 to 18.902 ± 0.001 and 15.653 to 15.702 ± 0.001 (Table 2). Our $^{206}Pb/^{204}Pb$ and $^{207}Pb/^{204}Pb$ values are very similar to those obtained by Stos-Gale (1992) from the Serifos granodiorite (Kefala site, i.e., 18.882 to 18.870 and 15.636 to 15.699) (Fig. 6).

DISCUSSION

Physicochemical conditions of native bismuth formation

Physicochemical conditions of Moutoulas mineralization were estimated from phase-stability relationships using SUPCRT92 (Johnson et al. 1992) with thermodynamic properties from the 2007 database (slop07.dat; Shock and Helgeson 1998). Reactions used to estimate these conditions and values of physicochemical parameters calculated using them are presented in Table 3. The corresponding phase relationships are illustrated graphically on pH vs. $\log f_{O_2}$ plots calculated for temperatures of 250 and 200 °C (Figs. 7a and 7b). These temperatures represent those estimated previously for stage I and stage IV, respectively (Supplemental[1] Tables 2, 3, and 4; Table 2). All solids and gas species were considered behave ideally. Individual ion activity coefficients of dissolved species were calculated using the B-γ extension of Helgeson et al. (1981) for an ionic strength (I) of 0.2.

The formation of sericite after orthoclase and albite in the inner alteration zone of the CBU schists require weakly acidic conditions during stage I (reactions 1 to 3, Table 3). A $\log(\alpha_{K^+}/\alpha_{Na^+})$ value of 0.73, at 250 °C, was calculated based on the equilibrium between orthoclase and albite (reaction 3). The $\log(\alpha_{K^+}/\alpha_{H^+})$ and $\log(\alpha_{Na^+}/\alpha_{H^+})$ values obtained from reactions 1 and 2 are 3.7 and 2.4, and so the calculated $\log\alpha_{Na^+}$ value is –0.47. The pH of the ore solution obtained from these values is 5.4.

A $\log f_{S_2}$ value of –13.8 ± 0.2 (PP-0.8, where PP is the pyrite-pyrrhotite buffer) was calculated for stage I from the pyrite and pyrrhotite equilibrium (reaction 4, Table 3). The maximum X_{FeS} content of sphalerite coexisting with pyrite, for this stage is 25.8% and the calculated $\log f_{S_2}$ value is –14.1 ± 0.2 (PP-1.1) based on the equation of Barton and Skinner (1979). Using compositional data for the gas phase in the fluid inclusions (Supplemental[1] Table 3; reaction 5 in Table 3) and the equations of McCartney and Lanyon (1989), we were also able to calculate the corresponding $\log f_{O_2}$ (–39.2 or HM-2.1, where HM is the hematite-magnetite buffer) (Fig. 7a).

By stage IV, the temperature had decreased to 200 °C, $\log f_{S_2}$ decreased to –16.5 ± 0.5 (PP-1.4) and $\log f_{O_2}$ to –43.5 (HM-3.5) (Fig. 7b). The value of $\log f_{S_2}$ was calculated from thermodynamic data for reaction 6, which describes the replacement of bismuthinite by native Bi, a common occurrence in late sub-stage IV. The value of $\log f_{O_2}$ was determined from compositional data for the gas phase in fluid inclusions as mentioned above for stage I (Table 3). The pH of the fluid

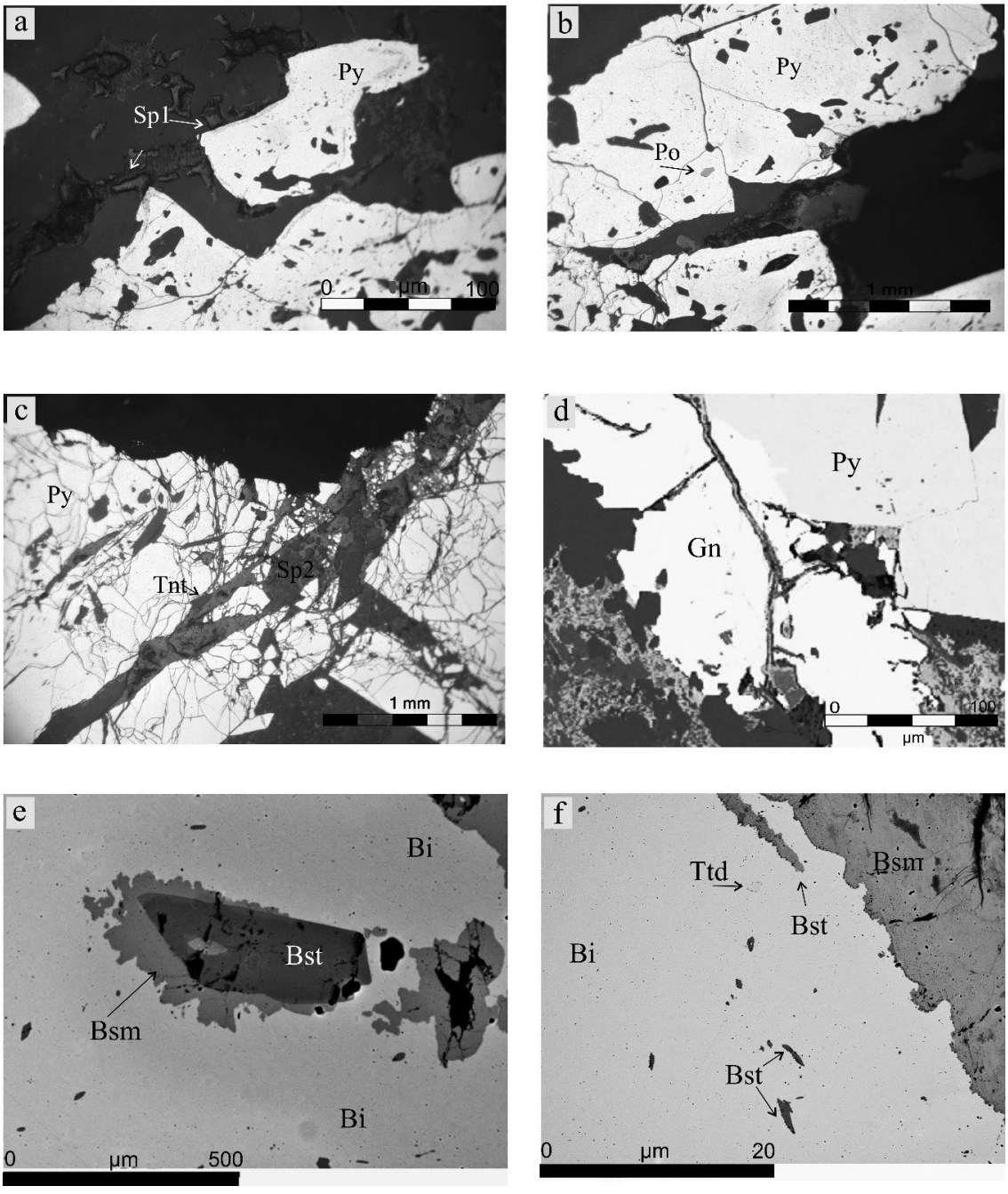

Figure 3. Reflected light and backscattered electron images. (**a**) Stage I pyrite (Py) and sphalerite (Sp1) (scale bar = 1 μm). (**b**) Stage I pyrite (Py) with pyrrhotite (Po) (reaction 4, Table 3, scale bar = 1 mm). (**c**) Stage II sphalerite (Sp2) and tetrahedrite-tennantite solid solutions (Tnt) filling fractures in brecciated stage I pyrite (Py) (scale bar = 1 mm). (**d**) Stage III galena (Gn) after stage I pyrite (Py) (scale bar = 100 μm). (**e**) Late sub-stage IV native Bi (Bi) that replaced early sub-stage IV bismuthinite (Bst) (reaction 7, Table 3). Both minerals were partially oxidized to bismite (Bsm) (scale bar = 500 μm). (**f**) Late sub-stage IV native Bi (Bi) after early sub-stage IV bismuthinite (Bst) and middle-sub-stage tetradymite. Native Bi was oxidized to bismite (Bsm) (reactions 14 and 15, Table 3) (scale bar = 20 μm).

(6.5) and the $\log\alpha_{HS^-_{(aq)}}$ and $\log\alpha_{H2S(aq)}$ values (–2.9 and –3.7) were calculated using the equilibrium constants for reactions 7, 8, and 9 for the $\log f_{O_2}$ and $\log f_{S_2}$ values referred to above (Table 3). A value of $\log f_{Te2(g)}$ (–17.0) was calculated from a combination of reactions 10, 11, and 12. Increased $\log f_{Te_{2(g)}}$, $\log\alpha_{H_2Te(aq)}$, and $\log\alpha_{HTe^-_{(aq)}}$ values is suggested to be responsible for the formation of tellurides (e.g., hessite and tetradymite) via reactions like 10 and 13 (Table 3).

During supergene alteration oxidation of native Bi (reaction 14) produced $Bi(OH)^{2+}$ ions as the dominant dissolved species in solu-

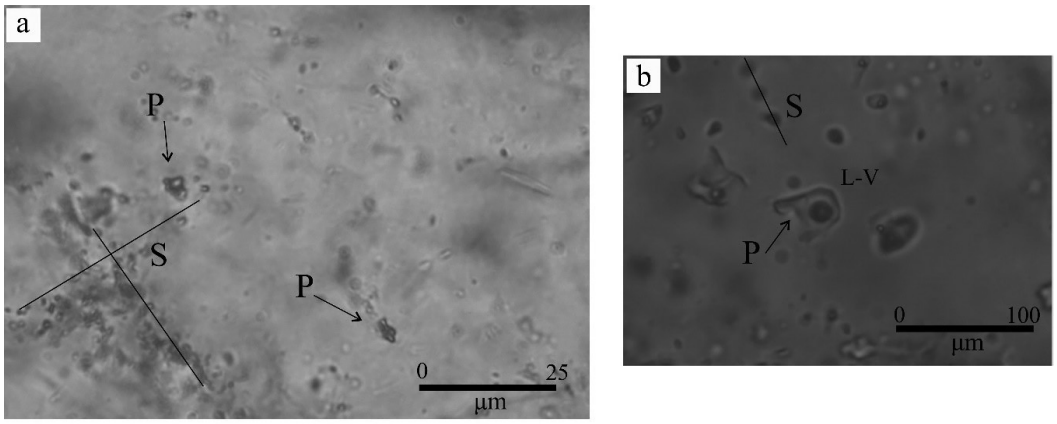

FIGURE 4. Photomicrographs of multiple fluid inclusion assemblages: (**a**) primary two-phase L-V (P) and secondary L-V (S) inclusions. The primary inclusions occur individually or as small, randomly oriented clusters, whereas the secondary fluid inclusions form trails that are aligned along fractures and terminate at crystal growth surfaces (scale bar = 25 μm). (**b**) Detail of **a** showing the primary inclusions with low V-L ratios (vapor bubble occupies up to ~20 vol%) used for Raman spectroscopy (scale bar = 100 μm).

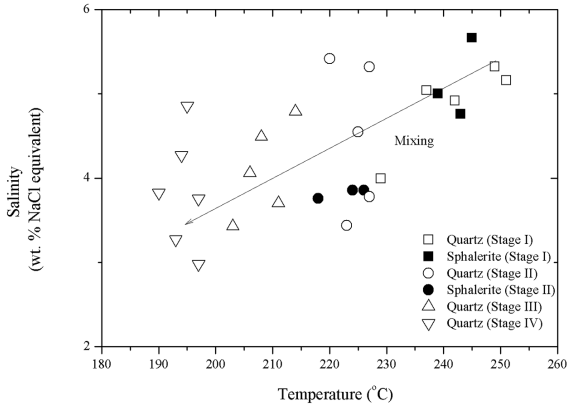

FIGURE 5. Liquid-vapor trapping temperature vs. salinity plot in the system NaCl-H_2O.

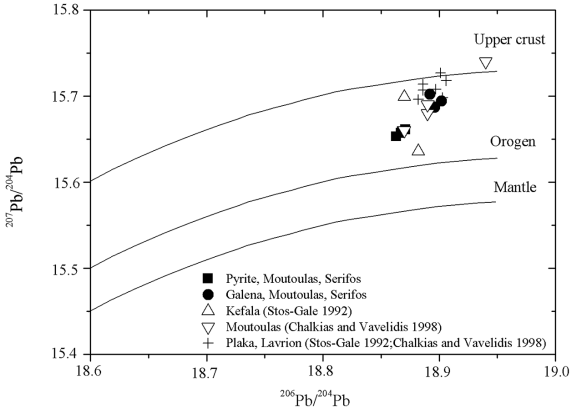

FIGURE 6. A plot of $^{206}Pb/^{204}Pb$ vs. $^{207}Pb/^{204}Pb$ using age-corrected data. The galena crystals analyzed in this study plot between the "Orogene" and "Upper Crust" curves. The "Upper Crust," "Orogene," and "Mantle" were based on the model of Zartman and Doe (1981). Also shown are samples of galena from the Kefala pluton (Stos-Gale 1992) and the Moutoulas mineralization (Chalkias and Vavelidis 1998).

TABLE 2. Sulfur and lead isotope data for pyrite, sphalerite, chalcopyrite, greenockite, and galena from the Moutoulas vein system, Serifos

Sample	Mineral	$\delta^{34}S$	T[a] (°C)	$\delta^{34}S_{H_2S}$[b]	$^{206}Pb/^{204}Pb$	$^{207}Pb/^{204}Pb$
SE1	Pyrite (stage I)[A]	4.83	249	2.28	18.863	15.653
SE2	Pyrite (stage I)[A]	3.78	249	3.33	18.867	15.657
SE3	Pyrite (stage I)	4.44	249	2.94	18.871	15.661
SE4	Pyrite (stage I)	4.12	249	2.62	18.868	15.659
SE1	Sphalerite (stage I)[A]	3.73	249	3.33	–	–
SE2	Sphalerite (stage I)[A]	2.69	249	2.29	–	–
SE3	Sphalerite (stage II)[B]	3.54	226	3.14	–	–
SE2	Chalcopyrite (stage I)	5.08	249	4.88	–	–
SE3	Greenockite (stage II)[B]	5.49	226	4.79	–	–
SE1	Galena (stage III)	5.62	200	3.02	18.896	15.687
SE2	Galena (stage III)	5.04	200	2.44	18.902	15.694
SE3	Galena (stage III)	5.37	200	2.77	18.892	15.702

[a] Temperatures obtained from fluid inclusion data, the CO_2-, CO_2/H_2S-, and Na-K-Ca geothermometers (Tables 3 and 4) and the pyrite-sphalerite (marked by [A]) and sphalerite-greenockite (marked by [B]) pairs; according to the equations of Ohmoto and Rye (1979), Ohmoto and Lasaga (1982), and Li and Liu (2006).
[b] Utilizing the H_2S-sulfide equations of Ohmoto and Rye (1979), Ohmoto and Lasaga (1982), and Li and Liu (2006).

tion. This reaction is promoted by higher $\log f_{O_2}$ values (–32.5 or HM+10) and a further decrease of pH of 7.1 (Table 3). The formation of bismutite [$(BiO_2)_2CO_3$] and bismite (Bi_2O_3) was likely promoted by a reaction similar to 15 (Table 3).

Source of metals and depositional controls

Skarn formation, at Serifos, evolved from high-temperature magnetite ores to retrograde replacement and vein mineralization that culminated with the deposition of native bismuth. Figure 5 shows that the decrease in temperature from stage I (~250 °C) to stage IV (~190 °C) was accompanied by a roughly linear decrease in salinity from ~5.7 to 1.3 wt% NaCl equivalent. This trend suggests dilution of the ore fluid as a result of mixing with waters of meteoric origin. Mixing of the ore fluid with oxidizing meteoric waters is also suggested by the gas chemistry, i.e., an increase of the $\log X_{O_2/H_2O}$ ratios from –3.4

TABLE 3. Reactions and corresponding values of selected physicochemical parameters applicable to the mineralizing fluid at Moutoulas, for temperatures of 250, 200, and 25 °C and an ionic strength I = 0.20

	Reaction	*T* (°C)	Calculated physicochemical parameters
1	$3KAlSi_3O_{8(s)} + 2H^+_{(aq)} = KAl_2Si_3O_{10}(OH)_{2(s)} + 6SiO_{2(aq)} + 2\ K^+_{(aq)}$	250[A]	$\log(\alpha_{K+}/\alpha_{H+}) = 3.7$, pH = 5.4
2	$3NaAlSi_3O_{8(s)} + 2H^+_{(aq)} + K^+_{(aq)} = KAl_3Si_3O_{10}(OH)_{2(s)} + 6SiO_{2(aq)} + 3Na^+_{(aq)}$	250[A]	$\log(\alpha_{Na+}/\alpha_{H+}) = 2.4$, pH = 5.4
3	$NaAlSi_3O_{8(s)} + K^+_{(aq)} = KAlSi_3O_{8(s)} + Na^+_{(aq)}$	250[A]	$\log(\alpha_{K+}/\alpha_{Na+}) = 0{,}73$, pH = 5.4
4	$2FeS_{2(s)} = 2FeS_{(s)} + S_{2(g)}$	250[A]	$\log f_{S_{2(g)}} = -13.8$
5	$2H_2O_{(g)} = O_{2(g)} + 2H_{2(g)}$	250[A], 200[B]	$\log f_{O_{2(g)}} = -39.2$ and -43.5
6	$Bi_2S_{3(s)} = 2Bi_{(s)} + 1.5S_{2(g)}$	200[B]	pH = 6.5
7	$2Bi_2S_{3(s)} + 6H_2O_{(l)} = 4Bi_{(s)} + 6H^+_{(aq)} + 6HS^-_{(aq)} + 6O_{2(g)}$	200[B]	$\log f_{S_{2(g)}} = -16.5$
8	$H_2S_{(aq)} = H^+_{(aq)} + HS^-_{(aq)}$	250, 200[B]	$\log a_{HS^-_{(aq)}} = -1.8$ and -2.9
9	$2H_2S_{(aq)} + O_{2(g)} = S_{2(g)} + 2H_2O_{(l)}$	250, 200[B]	$\log a_{HS^-_{(aq)}} = -1.8$ and -2.9
10	$Ag_2Te_{(s)} + H_2O_{(l)} = 2Ag_{(s)} + H_2Te_{2(aq)} + 0.5O_{2(g)}$	200[B]	$\log a_{H_2Te^-_{(aq)}} = -5.2$
11	$2H_2Te_{(aq)} + O_{2(g)} = Te_{2(g)} + 2H_2O_{(l)}$	200[B]	$\log f_{Te_{2(g)}} = -17.0$
12	$H_2Te_{(aq)} = H^+_{(aq)} + HTe^-_{(aq)}$	200[B]	$\log a_{HTe^-_{(aq)}} = -3.8$
13	$2Bi(OH)^{2+}_{(aq)} + 2H_2Te_{(aq)} + H_2S_{(aq)} = B_{i2}Te_2S_{(s)} + 4H_2O_{(l)} + 2H^+_{(aq)}$	200[B]	$\log a_{H_2S^-_{(aq)}} = -3.7$
14	$2Bi_{(s)} + 1.5O_{2(g)} + 4H^+_{(aq)} = 2Bi(OH)^{2+}_{(aq)} + H_2O_{(l)}$	250[A], 200[B], 25	$\log a_{Bi(OH)^{2+}_{(aq)}} = -14.0, -11.2, -10.3$. pH = 7.1
15	$4Bi(OH)^{2+}_{(aq)} + HCO^-_{3(aq)} + O_{2(g)} + H_2O_{2(l)} = (BiO_2)_2CO_{3(s)} + Bi_2O_{3(s)}$	25	$\log f_{O_{2(g)}} = -32.5$

Notes: [A] 250 and [B] 200 °C, temperatures based on fluid inclusions, the CO_2-, CO_2/H_2S-, and Na-K-Ca-geothermometers, and pyrite-sphalerite and sphalerite-greenockite isotopic pairs (Tables 3, 4, and 5). The thermodynamic properties of bismuth complexes were compiled from Skirrow and Walshe (2002), Tooth et al. (2008, 2011), Staude et al. (2012), and Zhou et al. (2016). For reactions 5, 11, 12, 13, 14, and 15 the logK values are –5.2, –4.7, –1.1, +11.7, +6.9, and –12.6, respectively.

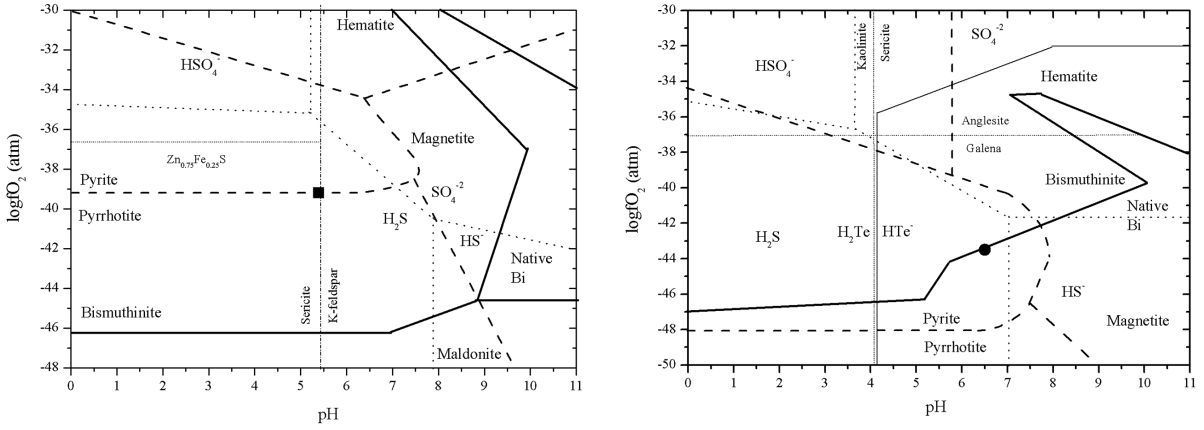

FIGURE 7. (**a**) Logf_{O_2} vs. pH plot for 250 °C, representing stage I of the Moutoulas skarn and vein mineralization. The dashed lines define the stability fields for pyrite (FeS_2), pyrrhotite (FeS), hematite (Fe_2O_3), and magnetite (Fe_3O_4). The Fe-S-O mineral boundaries are shown for ΣS = 0.1 mol/kg H_2O. Also shown are the sulfur species in the system H-S-O (dotted lines), the stability boundary for muscovite-K-feldspar (short-dash-dotted line), and the stability fields for bismuthinite, maldonite (Au_2Bi), and native bismuth (thick solid lines) fields. (**b**) Logf_{O_2} vs. pH plot for 200 °C, representing stage IV of the Moutoulas skarn mineralization. The dashed lines define the stability fields for pyrite (FeS_2), pyrrhotite (FeS), hematite (Fe_2O_3), and magnetite (Fe_3O_4). The Fe-S-O mineral boundaries are shown for ΣS = 0.1 mol/kg H_2O. The thin dotted and thin solid lines are the calculated contours for the sulfur and tellurium species in solution. Also shown are the stability boundaries for kaolinite-sericite (short-dash-dotted line) and anglesite-galena (short-dotted lines) and the stability fields for the sulfur species in the system H-S-O (dotted lines), and bismuthinite-native bismuth (thick solid lines). Data from Barton and Skinner (1979), Simon and Essene (1996), Afifi et al. (1988), Skirrow and Walshe (2002), Tooth et al. (2008, 2011), and Staude et al. (2012) were employed to calculate the Bi mineral stability fields in the two diagrams.

to –2.8 (Pearce et al. 2004) (Supplemental[1] Table 3).

The sulfur isotope data yielded a narrow range of calculated $\delta^{34}S_{H_2S}$ values, i.e., from 2.3 to 4.9‰ (Table 2). Such $\delta^{34}S_{H_2S}$ values reflect a dominantly magmatic source for the Bi-bearing mineralizing fluid. Further support is provided by the lead isotope data (Table 2) that suggest a mixed "Orogene" and "Upper Crust" source (Fig. 6). This implies that lead most probably derived from the Serifos pluton, which concurs with the lead data provided by Stos-Gale (1992). Pyrite, tetrahedrite-tennantite solid solutions, and galena from stages I, II, and III of the Moutoulas mineralization contain Bi, indicating that this element was incorporated during retrograde skarn formation and at early stages of the vein-type mineralization. This is consistent with the fact that the Serifos pluton appears relative enriched in Bi toward its margins (e.g., up to ~60%, Seymour et al. 2009). The Serifos skarn resembles the Lavrion (Greece), Stan Terg (Kosovo), and Wittichen Schwarzwald (Germany) Bi-bearing skarns. In these skarns, Bi is thought to be related to fluids derived from or equilibrated with a granodiorite during the retrograde skarn phase (Fig. 6, Voudouris et al. 2008a, 2008b; Kołodziejczyk et al. 2015; Staude et al. 2012).

The effects of temperature and pH on the solubility of $Bi(OH)^{2+}$ ions are summarized in a temperature vs. pH plot (Fig. 8). Calculation of the contours of the mass of $Bi(OH)^{2+}$ in solution was based on reaction 14 and the temperature, pH, log f_{O_2}, log f_{S_2}, and α_{H_2S} values obtained for stages I and IV. Saturation of $Bi(OH)^{2+}$ is evident as the mass of $Bi(OH)^{2+}$ in solution decreases from T = 250 to T = 200 °C (Fig. 8). Here it is suggested that the conditions of stage I (lower pH and higher f_{S_2} and f_{O_2}), favored the formation of Bi-enriched sulfides rather than the deposition of native bismuth. The proposed conditions for this stage lie within

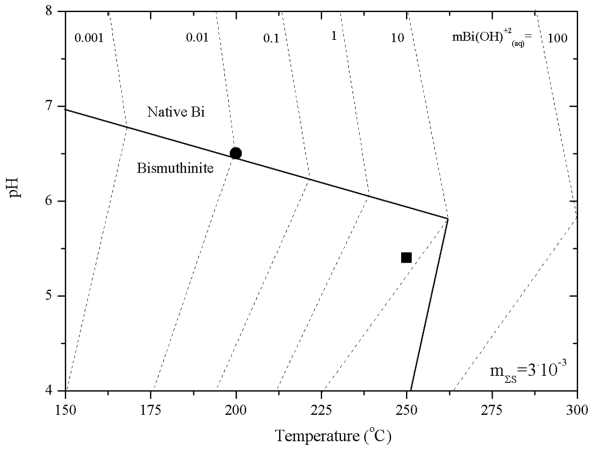

FIGURE 8. Temperature vs. pH plot summarizing changes in solubility of $Bi(OH)^{2+}$ ions (squares represent stage I and cycles stage IV). Calculation of the contours of mass in solution of $Bi(OH)^{2+}$ (in parts per million) was based on reaction 14, for $\log\alpha_{H_2S} = -3.7$ and $\log\alpha_{\Sigma S} = -3.0$, and the $\log f_{O_2}$ and $\log f_{S_2}$ values obtained for stages I and IV. Also shown are the stability boundary bismuthinite and native bismuth (thick solid line).

the stability fields of bismuthinite and pyrite, which show a broad overlap (Fig. 7a). At these conditions, as the ore solution was undersaturated in Bi (Fig. 8), the available Bi cannot form native bismuth and either is incorporated in the crystal lattice of the precipitated sulfides or forms submicroscopic grains within them (e.g., in pyrite and tetrahedrite, Supplemental[1] Table 1).

During stage IV native bismuth formed via reaction 7 that was controlled by the interplay of six physicochemical parameters. Temperature decrease, pH neutralization, f_{Te_2} increase coupled with decrease of f_{S_2}, α_{H_2S} (X_{H_2S} values decrease, Supplemental[1] Table 3), and f_{O_2} created a favorable environment for the precipitation of bismuthinite, then Bi-bearing tellurides, and native bismuth (Fig. 7b). At these more reducing and less acidic conditions the solubility of bismuth decreased (e.g., the $\log\alpha_{Bi(OH)^{2+}}$ values increased from –14.0 to –11.2, Table 3, Fig. 8) thus leading to the precipitation of native bismuth.

We propose that variation of temperature, pH, $\log f_{S_2}$, α_{H_2S}, $\log f_{O_2}$, and $\log f_{Te_2}$ was related to fluid-rock interaction and subsequent dilution of the ore fluid (Fig. 6). At Moutoulas open hydrothermal system, interaction of the Bi-bearing fluid with the intensely fractured CBU marbles also led to the enrichment of the mineralizing fluid in HCO_3^- ions (Supplemental[1] Table 4). Then supergene exposure and oxidation of the mineralization (e.g., $HCO_{3(aq)}^-$ anions required for reaction 15) may have resulted due to the intense exhumation and uplifting of the hydrothermal system (as it is suggested by Grasemann and Petrakakis 2007).

IMPLICATIONS

Herein we examine native bismuth in the Serifos skarn and the conditions under which it may be precipitated. We suggest that proximity to a granodiorite, the development of magnetite ores and subsequent retrograde sulfide mineralization played important role in the precipitation of native bismuth, and we propose that in such a hydrothermal environment ($T \approx 200$ °C) there are six parameters, i.e., temperature, pH, $\log f_{S_2}$, α_{H_2S}, $\log f_{O_2}$, and $\log f_{Te_2}$ that control native bismuth precipitation. We find that wall-rock interaction and dilution of Bi-bearing magmatic fluids, i.e., containing $Bi(OH)_{(aq)}^{2+}$, promoted native Bi saturation (Fig. 8) as these fluids facilitated a decrease in the mass of $Bi(OH)^{2+}$ ions in solution. We also propose that the formation of $Bi(OH)_x^{3-x}(HCO_3)_y^{3-y}$ complexes could play an important role on transporting this strategic element during wall-rock interaction. Destabilization of these complexes during dilution of the ore fluid via a probable reaction could be a mechanism controlling native bismuth precipitation:

$$Bi(OH)_2(HCO_3)_{(aq)} = Bi(OH)_{(aq)}^{2+} + HCO_{3(aq)}^- = Bi_{(s)} + 2H_2O_{(l)} + 2CO_{2(g)}.$$

ACKNOWLEDGMENTS

We kindly thank D. Katsikis for his assistance with sampling in the Moutoulas mine. Critical comments from J. Mavrogenes, P. Voudouris, and the Associate Editor J. Roberge, as well as an anonymous reviewer, are gratefully acknowledged.

REFERENCES CITED

Afifi, A.M., Kelly, W.C., and Essene, E.J. (1988) Phase relations among tellurides, sulfides, and oxides: I. Thermochemical data and calculated equilibria. Economic Geology, 83, 377–294.

Altherr, R., Kreuzer, H., Wendt, I., Lenz, H., Wagner, G.A., Keller, J., Harre, W., and Hohndorf, A. (1982) A late Oligocene/Early Miocene high temperature belt in the Attico-Cycladic crystalline complex (SE Pelagonia, Greece). Geologisches Jahrbuch, 23, 971–164.

Arnórsson, S., and Gunnlaugsson, E. (1985) New gas geothermometers for geothermal exploration-Calibration and application. Geochimica and Cosmochimica Acta, 49, 1307–1325.

Bakker, R.J. (2012) Package FLUIDS. Part 4: Thermodynamic modelling and purely empirical equations for H_2O-NaCl-KCl solutions. Mineralogy and Petrology, 105, 1–29.

Barton, P.B. Jr., and Skinner, B.J. (1979) Sulfide mineral stabilities. In H.L. Barnes, Ed., Geochemistry of the Hydrothermal Ore Deposits, 3rd ed., p. 236–333. Wiley, New York.

Beaudoin, G., and Therrien, P. (2009) The updated web stable isotope fractionation calculator. In P.A. De Groot, Ed., Handbook of Stable Isotope Analytical Techniques, Volume II, Elsevier, 1120–1122.

Bolhar, R., Ring, U., and Allen, C.M. (2010) An integrated zircon geochronological and geochemical investigation into the Miocene plutonic evolution of the Cyclades, Aegean Sea, Greece: Part 1: Geochronology. Contributions to Mineralogy and Petrology, 160, 719–742.

Brichau, S., Thomson, S.N., and Ring, U. (2010) Thermochronometric constraints on the tectonic evolution of the Serifos detachment, Aegean Sea, Greece. International Journal of Earth Sciences, 99, 379–393, DOI:10.1007/s00531-008-0386-0.

Bröcker, M., and Franz, L. (2005) P-T conditions and timing of metamorphism at the base of the Cycladic Blueschist unit, Greece: The Panormos window on Tinos re-visited. Neues Jahrbuch für Mineralogie Abhandlungen, 181, 91–93.

Brown, P.E. (1989) FLINCOR: A microcomputer program for the reduction and investigation of fluid inclusion data. American Mineralogist, 74, 1390–1393.

Chalkias, S., and Vavelidis, M. (1998) Interpretation of lead-isotope data from Greek Pb-Zn deposits, based on an empirical two-stage model. Bulletin of Geological Society of Greece, 23, 177–193.

Cook, N.J., Ciobanu, C.L., Spry, P.G., Voudouris, P., and the participants of the IGCP-486 (2009) Understanding gold-(silver)-telluride-(selenide) mineral deposits. Episodes, 32, 249–263.

Dhamelincourt, P., Beny, J.M., Dubessy, J., and Poty, B. (1979) Analyse d' inclusions fluids à la microsonde mole à effet Raman. Bulletin Mineralogie, 102, 600–610.

Ducoux, M., Branquet, Y., Jolivet, L., Arbaret, L., Grasemann, B., Rabillard, A., Gumiaux, C., and Drufin, S. (2017) Synkinematic skarns and fluid drainage along detachments: The West Cycladic Detachment System on Serifos Island (Cyclades, Greece) and its related mineralization. Tectonophysics, 695, 1–26.

Etschmann, B.E., Liu, W., Pring, A., Grundler, P.V., Tooth, B., Borg, S., Testemale, D., Brewe, D., and Brugger, J. (2016) The role of Te(IV) and Bi(III) chloride complexes in hydrothermal mass transfer: an X-ray absorption spectroscopic study. Chemical Geology, 425, 37–51.

Fournier, R.O., and Truesdell, A.H. (1973) An empirical Na-K-Ca geothermometer for natural waters. Geochimica et Cosmochimica Acta, 37, 1255–1275.

Frezzotti, M.L., Tecce, F., and Casagli, A. (2012) Raman spectroscopy for fluid inclusion analysis. Journal of Geochemical Exploration, 112, 1–20.

Fritz, P., Drimmie, R.J., and Norwick, K. (1974) Preparation of sulfur dioxide for mass spectrometer analysis by combustion of sulfide with copper oxide. Analytical Chemistry, 76, 164–166.

Grasemann, B., and Petrakakis, K. (2007) Evolution of the Serifos metamorphic

complex. In G. Lister, M. Forster, and U. Ring, Eds., Inside the Aegean Metamorphic Core Complexes. Journal of the Virtual Explorer, 28, 1–18.
Grasemann, B., Schneider, D.A., Stockli, D.F., and Iglseder, C. (2012) Miocene bivergent crustal extension in the Aegean: Evidence from the western Cyclades (Greece). Lithosphere, 4(1), 23–39, DOI:10.1130/L164.1.
Helgeson, H.C., Kirkham, D.H., and Flowers, G.C. (1981) Theoretical prediction of the thermodynamic behavior of aqueous electrolytes at high pressures and temperatures, Calculation of activity coefficients, osmotic coefficients, and apparent molal and standard and relative partial molal properties to 600 °C and 5kb. American Journal of Science, 281, 1249–1516.
Henley, R.W., Mavrogenes, J.A., and Tanner, D. (2012) Sulfosalt melts and heavy metal (As-Sb-Bi-Sn-Pb-Tl) fractionation during volcanic gas expansion: the El Indio (Chile) paleo-fumarole. Geofluids, DOI:10.1111/j.1468-8123.2011.00357.x.
Johnson, J.W., Oelkers, E.H., and Helgeson, H.C. (1992) SUPCRT92, A software package for calculating the standard molal thermodynamic properties of minerals, gases, aqueous species and reactions from 1 to 5000 bars and 0 to 1000 °C. Computer Geoscience, 18, 899–947.
Kołodziejczyk, J., Pršek, J., Melfos, V., Voudouris, P., Maliqi, F., and Kozub-Budzyń, G. (2015) Bismuth minerals from the Stan Terg deposit (Trepça, Kosovo). Mineralogical contribution to the evolution of the deposit. Neues Jahrbuch für Mineralogie, 192, 317–333.
Li, Y., and Liu, J. (2006) Calculation of sulfur isotope fractionation in sulfides. Geochimica et Cosmochimica Acta, 70, 1789–1795.
Mavrogenes, J.A., Henley, R.W., Reyes, A.C., and Berger, B. (2010) Sulfosalt melts: evidence of high temperature vapor transport of metals in the formation of high sulfidation lode gold deposits. Economic Geology, 105, 257–262.
McCartney, R.A., and Lanyon, G.W. (1989) Calculations of steam fractions in vapor-dominated geothermal systems using an empirical method. In 14th Annual Workshop on Geothermal Reservoir Engineering, Stanford, 155–161.
Nehring, N.L., and D'Amore, F. (1984) Gas chemistry and thermometry of the Cerro Prieto, Mexico, geothermal field. Geothermics, 13, 75–89.
Ohmoto, H., and Lasaga, A.C. (1982) Kinetics of reactions between aqueous sulfates and sulfides in hydrothermal systems. Geochimica et Cosmochimica Acta, 46, 1727–1745.
Ohmoto, H., and Rye, R.O. (1979) Isotopes of sulfur and carbon. In H.L. Barnes, Ed., Geochemistry of the Hydrothermal Ore Deposits, 3rd ed., 509–567. Wiley, New York.
Pearce, J.A., Czernichowski-Lauriol, I., Lombardi, S., Brune, S., Nador, A., Baker, J., Pauwels, H., Hatziyannis, G., Beaubien, S., and Faber, E. (2004) A review of natural CO_2 accumulations in Europe as analogues for geological sequestration. Geological Society, London, Special Publication, 233, 29–41.
Petrakakis, K., Zamoyli, A., Iglseder, C., Rambousek, C., Grasemann, B., Dragamits, E., and Photiadis, A. (2007) Geological map of Serifos. 1:50.000. Geological map of Greece, Institute of Geological and Mineralogical Exploration, Athens, Greece.
Rabillard, A., Arbaret, L., Jolivet, L., Le Breton, N., Gumiaux, C., Augier, R., and Grasemann, B. (2015) Interactions between plutonism and detachments during metamorphic core complex formation, Serifos Island (Cyclades, Greece). Tectonics, 34, 1080–1106, DOI:10.1002/2014TC003650.
Roedder, E. (1984) Fluid inclusions. Reviews in Mineralogy, 12, 550.
Salemink, J. (1985) Skarn and ore formation at Serifos, Greece as a consequence of granodiorite intrusion, 232 p. Ph.D. thesis, Geology Ultraiectina.
Seymour, K., Zouzias, D., Tombros, S.F., and Kolaiti, E. (2009) The geochemistry of the Serifos pluton and associated iron oxide and base metal sulphide ores: Skarn or metamorphosed exhalite deposits? Neues Jahrbuch für Mineralogie Abhandlungen, 186, 249–270, DOI:10.1127/0077-7757/2009/0143.
Shock, E.T., and Helgeson, H.C. (1998) Calculation of the thermodynamic and transport properties of aqueous species at high pressures and temperatures, Correlation algorithms for ionic species and equation of state prediction to 5 kb and 1000 °C. Geochimica et Cosmochimica Acta, 52, 2009–2036.
Simon, G., and Essene, E.J. (1996) Phase relations among selenides, sulfides, tellurides, and oxides: I. Thermodynamic properties and calculated equilibria. Economic Geology, 91, 1183–1208.
Skirrow, R.G., and Walshem, J.L. (2002) Reduced and oxidized Au-Cu-Bi iron oxide deposits of the Tennant Creek Inlier, Australia: an integrated geologic model. Economic Geology, 97, 1167–1202.
Staude, S., Werner, W., Mordhorst, T., Wemmer, K., Jacob, D.E., and Markl, G. (2012) Multi-stage Ag-Bi-Co-Ni-U and Cu-Bi vein mineralization at Wittichen, Schwarzwald, SW Germany: Geological setting, ore mineralogy, and fluid evolution. Mineralium Deposita, 47, 251–276, DOI:10.1007/s00126-011-0365-4.
Stos-Gale, A.Z. (1992) Application of lead isotope analysis to provenance studies in archaeology, 303 p. Ph.D. thesis, University of Oxford.
Stouraiti, C., and Mitropoulos, P. (1999) Variation in amphibole composition from the Serifos intrusive complex (Greece), under magmatic and hydrothermal alteration conditions. An application of hornblende geobarometry. Bulletin of Geological Society of Greece, 33, 39–50.
Tooth, B., Brugger, J., Ciobanu, C., and Liu, W. (2008) Modeling of gold scavenging by bismuth melts coexisting with hydrothermal fluids. Geology, 36, 815–818.
Tooth, B., Ciobanu, C.L., Green, L., O'Neill, B., and Brugger, J. (2011) Bi-melt formation and gold scavenging from hydrothermal fluids: an experimental study. Geochimica et Cosmochimica Acta, 75, 5423–5443.
Voudouris, P., Spry, P.G., Melfos, V., and Alfieris, D. (2007) Tellurides and bismuth sulfosalts in gold occurrences of Greece: mineralogy and genetic considerations. Geological Survey of Finland Guide, 53, 85–94.
Voudouris, P., Melfos, V., Spry, P.G., Bonsall, T., Tarkian, M., and Economou-Eliopoulos, M. (2008a) Mineralogy and fluid inclusion constraints on the evolution of the Plaka intrusion-related ore system, Lavrion, Greece. Mineralogy and Petrology, 93, 79–110.
Voudouris, P., Melfos, V., Spry, P.G., Bonsall, T., Tarkian, M., and Solomos, C. (2008b) Carbonate-replacement Pb-Zn-Ag±Au mineralization in the Kamariza area, Lavrion, Greece: Mineralogy and thermochemical conditions of formation. Mineralogy and Petrology, 94, 85–106.
Xypolias, P., Iliopoulos, I., Chatzaras, V., and Kokkalas, S. (2012) Subduction and exhumation related structures in the Cycladic Blueschists: insights from Evia Island (Aegean region, Greece). Tectonics, 31, TC2001, DOI:10.1029/2011TC002946.
Yardley, B.W.D., Banks, D.A., and Bottrell, S.H. (1993) Post-metamorphic gold-quartz veins from N.W. Italy: the composition and origin of the ore fluid. Mineralogical Magazine, 57, 407–422.
Yuan, H., Chen, K., Zhian, B., Zong, C., Dai, M., Fan, C., and Yin, C. (2013) Determination of lead isotope compositions of geological samples using femtosecond laser ablation MC-ICPMS. Chinese Science Bulletin, 58, 3914–3921.
Zartman, R.E., and Doe, B.R. (1981) Plumbotectonics. The Model. Tectonophysics, 75, 135–162.
Zhou, H., Sun, X., Fu, Y., Lin, H., and Jiang, L. (2016) Mineralogy and mineral chemistry of Bi-minerals: Constraints on ore genesis of the Beiya giant porphyry-skarn gold deposit, southwestern China. Ore Geology Reviews, 79, 408–424.

Manuscript received March 1, 2017
Manuscript accepted April 28, 2017
Manuscript handled by Julie Roberge